Sensitivity-based finite element model updating of a pontoon bridge

Ø.W. Petersen[a,*], O. Øiseth[a]

[a]NTNU, Norwegian University of Science and Technology, NO-7491 Trondheim, Norway

Abstract

Numerical models of large civil engineering structures are prone to errors and uncertain system parameters, which inevitably affect the ability of such models to accurately predict dynamic behaviour. Finite element (FE) model updating can be used to calibrate the numerical models towards the observed behaviour. In this paper, a case study of the sensitivity method in FE model updating is presented. The methodology is applied to the Bergsøysund Bridge, which is a long-span floating pontoon bridge in Norway. A system identification is performed based on acceleration data and thirty vibration modes are identified. The FE model is calibrated by reducing the difference between the identified and numerical natural frequencies and mode shapes of the bridge. The model uncertainties are parametrized with a total of 27 parameters. We demonstrate how an analytical sensitivity matrix can be constructed for floating structures, where the system mass and damping matrices are functions of frequency due to fluid-structure interaction. After updating, the mean error in natural frequencies is decreased from 3.23% to 2.34%, and the average MAC number is increased from 0.87 to 0.94. Although the largest errors are significantly reduced, the updated parameters are believed to be affected by noise from the system identification. Challenges related to the presence of very closely spaced vibration modes are also shown, in which matching the identified modes to the modelled modes becomes difficult. This study indicates that models of large bridges can be significantly improved, but many practical issues still exist.

Keywords: Floating bridge, finite element model updating, sensitivity method

1. Introduction

The analysis of large civil engineering structures for predicting dynamic behaviour is generally based on numerical finite element (FE) models. These models are typically idealized representations, which may involve modelling simplifications or system parameters that are uncertain, e.g. boundary conditions, geometry, material properties or kinematic interactions. One approach for reducing the uncertainties of numerical models is to perform a model calibration or updating when measurement data of the relevant structure are available [1]. FE model updating has become popular because of its ability to estimate unknown system parameters by matching the predicted behaviour to the

*Corresponding author
Email addresses: `oyvind.w.petersen@ntnu.no` (Ø.W. Petersen), `ole.oiseth@ntnu.no` (O. Øiseth)
URL: `https://www.ntnu.edu/kt/research/dynamics` (Ø.W. Petersen)

observed structural behaviour, which can often be measured under operational condition. Structural health monitoring and damage detection [2–10] are also growing fields for the application of updating tools. The comprehensive survey by Mottershead and Friswell [11] summarizes many of the current model updating techniques. A distinction between the two classes of global and local methods can be made [6]. Global methods directly modify the stiffness and mass matrices to better fit a set of reference data [12], but such methods have the clear disadvantage that the physical meaning behind the system alterations is hidden. Local or parametric methods correct the mass and stiffness matrices by linking them to physical model parameters that can be regarded as uncertain. Parametric methods are the preferred approach for case studies, where learning about the physical significance behind the model alterations is also an objective, for example, an unknown material property or damage in a component. A drawback is that the updating process is generally not a one-step procedure; rather, iterations are required. Sensitivity-based methods [5, 7, 13–19] are by far the most popular approach when the model is parametrized. A review of sensitivity methods is given by Link [20]. Response surface methods are another widely used alternative [21–23], but such methods can be costly to establish when a large number of updating parameters is considered.

Many engineering challenges are still encountered in FE model updating of large structures such as bridges. Updating applications to cable-stayed bridges [6, 24–29], suspension bridges [30–33] and other types of bridges [5, 15, 16, 34–37] are practical case studies found in the literature. Due to the scale of operation, ambient excitation is generally the preferred option when vibration measurements are performed. Using a vehicle with known axle loads in a controlled test is another option [38]. The errors in natural frequencies for very large bridges (prior to updating) are typically reported in the range 0-5%, although errors up to 10-20% for some modes are not unusual. The previous studies successfully demonstrate that a significant improvement of large FE models is attainable using simple model updating techniques.

Although updating of cable-stayed bridges and suspension bridges is well documented, it has not been attempted on floating bridges. Research on large floating bridges is an area that is largely unexplored since few such structures have been constructed; an overview can be found in [39]. In a review process of the E39 Coastal Highway Project in Norway, however, the use of pontoon bridges and suspension bridges with floating towers to cross fjords is considered. The designated fjords are 1-3 km wide, and thus, the new bridges will have very long spans. Long span lengths coupled with the non-conventional design concepts pose a design challenge. State-of-the-art understanding of floating bridge dynamic behaviour is required to safely design and construct the new bridges. The dynamic behaviour of floating bridges is determined not only by structural vibrations but also by fluid-structure interaction (FSI), which means that greater model uncertainties are expected than for a conventional dry structure. Therefore, learning more about the performance of similar existing bridges is desired.

One of the studied bridges is the Bergsøysund Bridge, which is a long-span pontoon bridge that only has end supports. A monitoring system is installed at the Bergsøysund Bridge to measure the dynamic activity and ambient conditions [40]. This bridge has already been subjected to previous research, including studies of stochastic load and response modelling [41], system identification [42] and studies on estimation of forces and response [43]. In this

Figure 1: Alongside view of the Bergsøysund Bridge. Photograph: K.A. Kvåle.

article, we demonstrate an application of the sensitivity method in model updating to a case study of the Bergsøysund Bridge. Herein, the methodology is tested on a system that has extremely closely spaced modes, which is a challenge when the modes of the measurement data are sought to be matched with the model. One characteristic that the Bergsøysund Bridge shares with other very large bridges is the presence of low natural frequencies. In these structures, many modes contribute to the total dynamic response under low-frequency ambient excitation, such as wind or wave loading. It is thus imperative to ensure that the numerical model is well calibrated towards multiple modes, which is an inquiry made in this case study. A strong motivation for performing model updating is that future studies of the bridge dynamics can be directly improved with higher confidence in the results.

In the presented approach, the system matrices are parametrized. We present a procedure for establishing an analytical sensitivity matrix for floating structures, which takes the FSI not encountered in formulations of ordinary structures into account. In the chosen updating objective, the natural frequencies and mode shapes are calibrated towards the observed dynamic behaviour in an iterative optimization problem. The updating parameters are limited to bounds set by engineering judgement.

2. Bridge description and system equations for floating bridges

The Bergsøysund Bridge, which is shown in Fig. 1, is located in mid-western Norway. Placed into service in 1992, this bridge was constructed as part of a larger infrastructural project connecting the archipelago cities to the mainland. The total length of the floating span is 840 m. The bridge has two main components: a steel superstructure and seven concrete pontoons. As shown in Fig. 2, the pontoons are distributed approximately 100 m apart. The superstructure consists of a plated bridge deck stiffened with trapezoidal profiles and a trusswork, which is connected to each pontoon by four ”feet”. The bottom chords and diagonals in the truss are circular tube profiles, whereas the top chord is a welded box profile. Since the bridge is only supported at the end abutments, it is particularly susceptible to dynamic excitation from ambient wave loading.

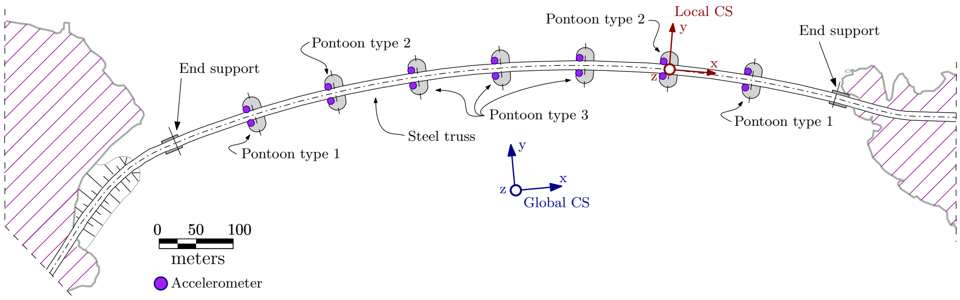

Figure 2: Plan view drawing of the Bergsøysund Bridge with the locations of the tri-axial accelerometers shown.

The dynamic behaviour of floating bridges can be formulated by the combination of the structural vibration and the dynamic interaction with the surrounding fluid. For a system with n_{DOF} degrees of freedom (DOFs), the equations of motion in a mixed time- and frequency-domain formulation are given as follows:

$$(\boldsymbol{M}_s + \boldsymbol{M}_h(\omega))\ddot{\boldsymbol{u}}(t) + (\boldsymbol{C}_s + \boldsymbol{C}_h(\omega))\dot{\boldsymbol{u}}(t) + (\boldsymbol{K}_s + \boldsymbol{K}_h)\boldsymbol{u}(t) = \boldsymbol{p}_w(t) \tag{1}$$

Here, $\boldsymbol{u} \in \mathbb{R}^{n_{DOF}}$ is the physical DOF vector and $\boldsymbol{p}_w(t) \in \mathbb{R}^{n_{DOF}}$ are wave forces. $\boldsymbol{M}_s$, $\boldsymbol{C}_s$ and $\boldsymbol{K}_s \in \mathbb{R}^{n_{DOF} \times n_{DOF}}$ are the structural mass, damping, and stiffness matrices, respectively. Furthermore, the following three hydrodynamic matrices account for the FSI: the added mass $\boldsymbol{M}_h(\omega) \in \mathbb{R}^{n_{DOF} \times n_{DOF}}$ and the potential damping $\boldsymbol{C}_h(\omega) \in \mathbb{R}^{n_{DOF} \times n_{DOF}}$ are frequency dependent, while the restoring stiffness $\boldsymbol{K}_h \in \mathbb{R}^{n_{DOF} \times n_{DOF}}$ is constant. For elaborations on the modelling of floating structures, we refer to [44]. In this paper, Eq. 1 is not applied directly but rather reformulated through two steps. The first step considers only a subsystem of Eq. 1:

$$\boldsymbol{M}_s\ddot{\boldsymbol{u}}(t) + (\boldsymbol{K}_s + \boldsymbol{K}_h)\boldsymbol{u}(t) = \boldsymbol{0} \tag{2}$$

The eigenvalue problem of the system in Eq. 2 is solved to obtain n_m mass-normalized modeshapes $\boldsymbol{\Phi} \in \mathbb{R}^{n_{DOF} \times n_m}$ and the matrix $\boldsymbol{\Omega} \in \mathbb{R}^{n_m \times n_m}$, which is populated diagonally with the frequencies. A reduced-order model with n_m modes is then constructed when the modal transform $\boldsymbol{u}(t) = \boldsymbol{\Phi}\boldsymbol{z}(t)$ is applied to Eq. 2:

$$\boldsymbol{I}\,\ddot{\boldsymbol{z}}(t) + \boldsymbol{\Omega}^2\boldsymbol{z}(t) = \boldsymbol{0} \tag{3}$$

In the second reformulation step, Eq. 1 is premultiplied with $\boldsymbol{\Phi}^T$:

$$\left(\boldsymbol{I} + \boldsymbol{\Phi}^T\boldsymbol{M}_h(\omega)\boldsymbol{\Phi}\right)\ddot{\boldsymbol{z}}(t) + \left(\boldsymbol{\Phi}^T\boldsymbol{C}_s\boldsymbol{\Phi} + \boldsymbol{\Phi}^T\boldsymbol{C}_h(\omega)\boldsymbol{\Phi}\right)\dot{\boldsymbol{z}}(t) + \boldsymbol{\Omega}^2\boldsymbol{z}(t) = \boldsymbol{\Phi}^T\boldsymbol{p}_w(t) \tag{4}$$

We then consider the terms $\boldsymbol{M}_{upd}$ and $\boldsymbol{K}_{upd} \in \mathbb{R}^{n_{DOF} \times n_{DOF}}$, which contain the added (or removed) mass and stiffness and are later calibrated in a model updating scheme. These two matrices are separated from the other system matrices to keep a clear and convenient formulation for updating. The modal forms of $\boldsymbol{M}_{\mathrm{upd}}$ and $\boldsymbol{K}_{\mathrm{upd}}$ are added to Eq. 4:

$$\left(\boldsymbol{I} + \boldsymbol{\Phi}^{\mathrm{T}}\boldsymbol{M}_{\mathrm{h}}(\omega)\boldsymbol{\Phi} + \boldsymbol{\Phi}^{\mathrm{T}}\boldsymbol{M}_{\mathrm{upd}}\boldsymbol{\Phi}\right)\ddot{\boldsymbol{z}}(t) + \left(\boldsymbol{\Phi}^{\mathrm{T}}\boldsymbol{C}_{\mathrm{s}}\boldsymbol{\Phi} + \boldsymbol{\Phi}^{\mathrm{T}}\boldsymbol{C}_{\mathrm{h}}(\omega)\boldsymbol{\Phi}\right)\dot{\boldsymbol{z}}(t) + \left(\boldsymbol{\Omega}^2 + \boldsymbol{\Phi}^{\mathrm{T}}\boldsymbol{K}_{\mathrm{upd}}\boldsymbol{\Phi}\right)\boldsymbol{z}(t) = \boldsymbol{\Phi}^{\mathrm{T}}\boldsymbol{p}_{\mathrm{w}}(t) \tag{5}$$

The above system formulation has the benefit of adding the hydrodynamic mass and damping together with the updating terms to a modally truncated system to reduce the computational burden and better suit an implementation in which the total model is constructed using several modelling tools, as will be explained below. The eigenvalue problem of Eq. 5, rewritten in state-space form, reads as follows:

$$\left[\begin{bmatrix} i\lambda_r & 0 \\ 0 & (i\lambda_r)^* \end{bmatrix} - \boldsymbol{A}(\omega_{d,r})\right]\begin{bmatrix} \boldsymbol{\psi}_r & \boldsymbol{\psi}_r^* \\ \boldsymbol{\psi}_r(i\lambda_r) & \boldsymbol{\psi}_r^*(i\lambda_r)^* \end{bmatrix} = \boldsymbol{0} \tag{6}$$

Here, $\boldsymbol{A}$ is the state matrix:

$$\boldsymbol{A}(\omega_{d,r}) = \begin{bmatrix} \boldsymbol{0} & \boldsymbol{I} \\ \boldsymbol{M}^{-1}(\omega_{d,r})\boldsymbol{C}(\omega_{d,r}) & \boldsymbol{M}^{-1}(\omega_{d,r})\boldsymbol{K} \end{bmatrix} \tag{7}$$

The problem in Eq. 6 can be solved iteratively; see Kvåle et al. [41] for details. Assuming sub-critical damping, the solution has conjugate eigenvector pairs $\boldsymbol{\psi}_r, \boldsymbol{\psi}_r^* \in \mathbb{C}^{\mathrm{n_m}}$ $(r = 1, 2 \ldots \mathrm{n_m})$ related to the complex eigenvalues $i\lambda_r, (i\lambda_r)^* \in \mathbb{C}$:

$$i\lambda_r, (i\lambda_r)^* = -\xi_r\omega_r \pm \sqrt{1-\xi_r^2}\,\omega_r i \tag{8}$$

Here, the natural frequency is ω_r and the critical damping ratio is ξ_r. The system matrices used in Eq. 7, in which the hydrodynamic matrices are evaluated at the damped natural frequency $\omega_{d,r} = \sqrt{1-\xi_r^2}\,\omega_r$, are defined as follows:

$$\boldsymbol{M}(\omega_{d,r}) = \boldsymbol{I} + \boldsymbol{\Phi}^{\mathrm{T}}\boldsymbol{M}_{\mathrm{h}}(\omega_{d,r})\boldsymbol{\Phi} + \boldsymbol{\Phi}^{\mathrm{T}}\boldsymbol{M}_{\mathrm{upd}}\boldsymbol{\Phi} \tag{9}$$

$$\boldsymbol{C}(\omega_{d,r}) = \boldsymbol{\Phi}^{\mathrm{T}}\boldsymbol{C}_{\mathrm{s}}\boldsymbol{\Phi} + \boldsymbol{\Phi}^{\mathrm{T}}\boldsymbol{C}_{\mathrm{h}}(\omega_{d,r})\boldsymbol{\Phi} \tag{10}$$

$$\boldsymbol{K} = \boldsymbol{\Omega}^2 + \boldsymbol{\Phi}^{\mathrm{T}}\boldsymbol{K}_{\mathrm{upd}}\boldsymbol{\Phi} \tag{11}$$

The eigenvectors $\boldsymbol{\psi}_r$ are collected in the matrix $\boldsymbol{\Psi} \in \mathbb{C}^{\mathrm{n_m}\times\mathrm{n_m}}$. For completeness, the physical DOF can then be reconstructed from two modal transformations:

$$\boldsymbol{u}(t) = \boldsymbol{\Phi}\boldsymbol{z}(t) = \boldsymbol{\Phi}\begin{bmatrix} \boldsymbol{\Psi} & \boldsymbol{\Psi}^* \end{bmatrix}\begin{bmatrix} \boldsymbol{y}(t) \\ \boldsymbol{y}^*(t) \end{bmatrix} \tag{12}$$

where a modal coordinate vector $\boldsymbol{y}(t) \in \mathbb{C}^{\mathrm{n_m}}$ was introduced. Note that the matrix $\boldsymbol{\Psi}$ is sensitive to the updating parameters, whereas $\boldsymbol{\Phi}$ is constant. A convergence assessment reveals that $\mathrm{n_m} = 100$ is a sufficient number of modes for the solution of Eq. 6 to stabilize. This high number of modes is needed since the hydrodynamic mass significantly

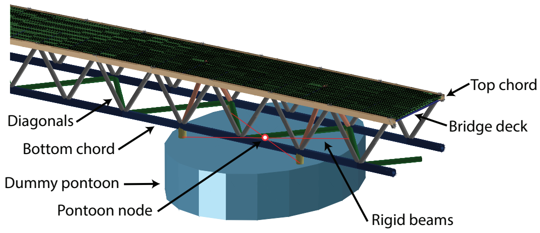

Figure 3: Section of the Abaqus FE model. The pontoon is a dummy object for visualization only, and the red cross is the model replacement for the rigidity of the pontoon.

contributes to the total mass, which implies that the modes for the wet system will be significantly different from the ones calculated in Eq. 3.

A brief description of the employed modelling tools follows; for details, we refer to [41]. Specifications in the technical drawings are used as the basis for constructing the models. The steel superstructure is modelled in the FE software Abaqus. Two-node Timoschenko beam elements (B32) are utilized for the truss, and eight-node shell elements (S8R) are used for the plated steel deck. It is assumed that a pontoon behaves as a rigid body, which is a fair simplification since the pontoons are very stiff compared to the remainder of the structure. The pontoons are therefore replaced by massless rigid beams in the FE model. To retain the correct inertia properties, the 6x6 pontoon mass matrix is lumped to the pontoon node; see Fig. 3. Each of the different pontoon types are modelled in DNV HydroD WADAM, which is a commercial software implementing linearized potential theory. From this program, the matrices $\boldsymbol{M}_{\mathrm{h}}(\omega)$, $\boldsymbol{C}_{\mathrm{h}}(\omega)$ and $\boldsymbol{K}_{\mathrm{h}}$ are obtained. For illustrative purposes, the added mass and damping for the midmost pontoons are plotted in Fig. 4. A strong frequency dependency is observed in the lower frequency range, and asymptotic values are reached for high frequencies. The hydrodynamic properties are also directly added to the pontoon nodes. For the damping originating from the structure, low damping ratios are realistic. A Rayleigh damping model is assumed:

$$\boldsymbol{C}_{\mathrm{s}} = \alpha\boldsymbol{M}_{\mathrm{s}} + \beta(\boldsymbol{K}_{\mathrm{s}} + \boldsymbol{K}_{\mathrm{h}}) \tag{13}$$

The coefficients $\alpha = 5\times10^{-3}$ and $\beta = 10^{-3}$ are used, which provide damping ratios of 0.2 to 0.8 % in the frequency range 0-15 rad/s. We refer to [41] for a description on how the two submodels (Abaqus and DNV HydroD WADAM) can be fused together.

3. Model updating parameters

Parametric approaches in model updating have the advantage of directly relating the parameters to the system matrices. It is preferred to retain a practical interpretation of the results and thus make the parameters physically meaningful. Next, a set of updating parameters is selected.

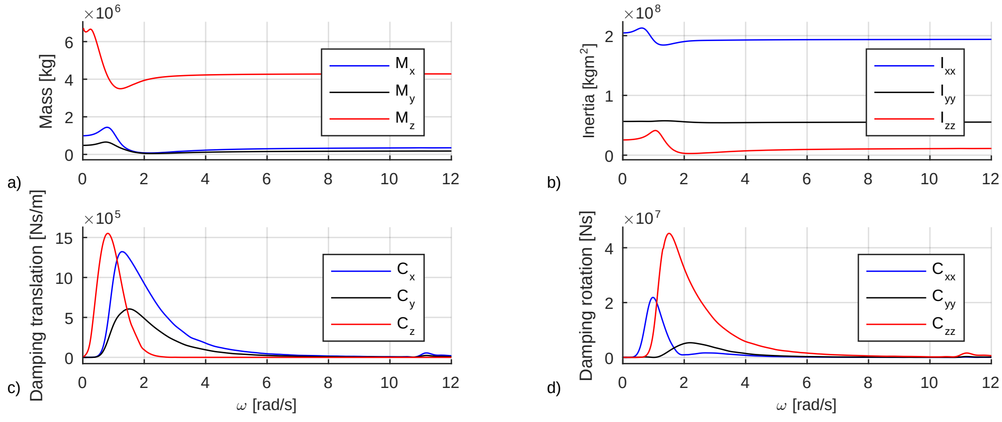

Figure 4: Added hydrodynamic mass (a), moment of inertia (b), damping in translation (c) and rotation (d) for pontoon type 3.

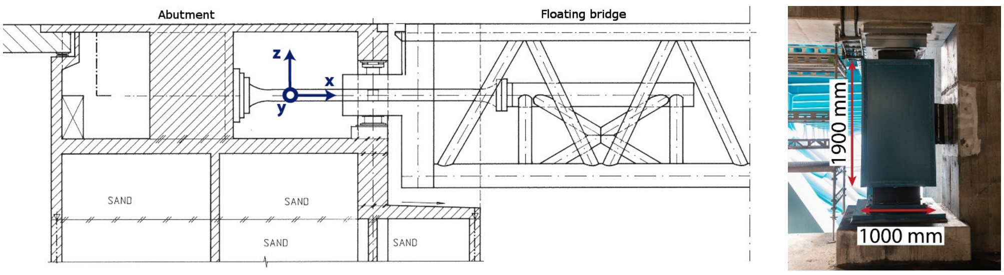

Figure 5: Left: technical drawing of end support; right: neoprene bearing

At each of the end supports, an axial rod and two neoprene bearings attach the steel superstructure to the concrete abutments, as shown in Fig. 5. Since the bridge is only supported at the ends, the stiffness of the bearings influences the global dynamic behaviour. In particular, the stiffness governs the torsional and horizontal modes since pontoons provide no lateral stiffness. The bearings are modelled as linear springs in the FE model. However, the spring stiffness has a high degree of uncertainty, which can be attributed not only to the neoprene material itself but also to unknown effects of the embedded steel plates and pretensioning. The idealization of a bearing as a single node can also cause errors. The bearing is parametrized by four stiffness parameters. The following 6x6 matrix is used to describe the stiffness:

$$\begin{bmatrix} k_x & 0 & 0 & 0 & 0 & 0 \\ 0 & k_y & 0 & 0 & 0 & 0 \\ 0 & 0 & k_z & 0 & 0 & 0 \\ 0 & 0 & 0 & k_{rx} & 0 & 0 \\ 0 & 0 & 0 & 0 & 0 & 0 \\ 0 & 0 & 0 & 0 & 0 & 0 \end{bmatrix} \tag{14}$$

Figure 6: Displacement mode of the bridge at one metre tide (scaled 10 times).

Here, k_x, k_y and k_z are translational spring constants, where the subscript indicates the direction in a local coordinate system. k_{rx} accounts for rotational stiffness. k_{ry} and k_{rz} have a negligible influence, and thus, they are excluded. The chosen stiffness model is applied to all four bearings because they are technically identical.

Although the truss geometry is well defined and the elastic modulus of steel is generally not uncertain, the global dynamic behaviour is highly sensitive to the properties of the steel superstructure. The flexibility of joints and effective beam lengths are typical sources of uncertainty in a beam element model. The two parameters η_{steel} and μ_{steel} are introduced to account for errors in the stiffness and mass of the steel superstructure. These parameters are used as scaling factors of the steel stiffness and mass submatrix, respectively. The mass parameter m_{deck}, distributed uniformly on the bridge deck, is introduced to account for modelling errors in, e.g. asphalt and steel railing. The initial model is given 135 kg/m^2 of non-structural mass, which has a total area of $11 \times 840 = 9240$ m^2.

Many of the uncertainties in the model can be attributed to the pontoons and the FSI. The pontoons are made from lightweight aggregate concrete, and variations in the density are typically in the range 2-5%. During finalization of the bridge, the pontoons were also ballasted with gravel until the desired draft was reached. The actual amount of ballast can therefore deviate from the quantity recommended in the technical drawings. A set of five inertia parameters for each of the three pontoon types, as illustrated in Fig. 2, is chosen. It is assumed that the mass deviation has two symmetry planes and has its mass centre shifted a distance dz from the pontoon node along a vertical axis, directed positively upwards. The following rigid body mass matrix is added locally to the pontoon nodes to calibrate the inertia:

$$\begin{bmatrix} m_i & 0 & 0 & 0 & -dz_i \cdot m_i & 0 \\ 0 & m_i & 0 & dz_i \cdot m_i & 0 & 0 \\ 0 & 0 & m_i & 0 & 0 & 0 \\ 0 & dz_i \cdot m_i & 0 & I_{xx,i} + dz_i^2 \cdot m_i & 0 & 0 \\ -dz_i \cdot m_i & 0 & 0 & 0 & I_{yy,i} + dz_i^2 \cdot m_i & 0 \\ 0 & 0 & 0 & 0 & 0 & I_{zz,i} \end{bmatrix} \tag{15}$$

m is a mass, I is a moment of inertia, and the subscripts x, y and z refer to a pontoon local coordinate system; ref. Fig. 2. The index $i = 1, 2, 3$ denotes the three different pontoon types. Although it is possible that deviations within one pontoon type could occur in reality, the classification is used to retain the symmetry of the model.

Next, the hydrodynamic contribution is considered. The mean difference between low and high tides at the site is 1.5 m, which means that the waterline level at the pontoons can vary. When static buoyancy forces are applied to the numerical model, the displacement pattern shown in Fig. 6 is observed. For a unit metre of tidal water increase, the five midmost pontoons are raised 1.04 m. The two outermost pontoons are restrained by the end supports and are only raised 0.74 m. The result is consistent with measurements of the waterline level performed at the site. Although changes in draft influence the terms $\boldsymbol{M}_{\mathrm{h}}(\omega)$ and $\boldsymbol{C}_{\mathrm{h}}(\omega)$, the sensitivity to the tidal water is very small since the pontoon displacement relative to the water plane is small. The largest changes in displaced water mass are at the ends, which generally have less influence on the dynamic behaviour. Including the tidal water level as a parameter is ruled unnecessary. The model is nevertheless still sensitive to possible errors in $\boldsymbol{M}_{\mathrm{h}}(\omega)$. Parameterizing the uncertainties from this term is difficult. For simplicity, a scale factor $\nu_{hydro,i}$ $(i = 1, 2, 3)$ is used to scale the hydrodynamic mass for the three pontoon types. For consistency, the damping term $\boldsymbol{C}_{\mathrm{h}}(\omega)$ is also scaled by the same factor.

For a rigid object that is floating freely, the restoring stiffness in rotation can be found in a straightforward manner by moment equilibrium in a state of unit rotation of the object. This is however not the case for a floating bridge where the pontoons are connected to the steel truss and are thus not allowed to rotate freely. Although basic assumptions can be made on the pontoon-truss displacement pattern, how the truss superstructure contributes to the rotational stiffness is uncertain. The parameter $K_{h,x,i}$ $(i = 1, 2, 3)$ is used to control the rotation stiffness about the x-axis (torsion). Rotation stiffness about the y-axis has an insignificant impact and is thus excluded from updating. Additionally, the vertical restoring stiffness $K_{h,z}$ is included as a parameter. It is considerably less uncertain than the rotation, but it has a major influence on the vertical modes and should thus be included. $K_{h,z}$ is made common for all pontoon types. The parameters related to hydrodynamics are assumed to be equal for pontoon types 2 and 3 (i.e. $\nu_{hydro,2} = \nu_{hydro,3}$, $K_{h,x,2} = K_{h,x,3}$) since these should have identical exterior geometries and waterline levels.

In total, the number of independent updating parameters is $\mathrm{n_p} = 27$. A list is presented in Table 1 and a normalized sensitivity plot is shown in Fig. 7. The sensitivity plot is produced for the initial model and the sensitivities can highly change throughout the updating process. Note that since many of the parameters are related to the properties of the pontoon node, it can in a practical sense become problematic to distinguish them from each other.

How this might affect the updating is addressed further in Section 6.

4. Model updating framework

The sensitivity method is chosen for updating; see, e.g., Mottershead et al. [19] for a tutorial. It is assumed that $\mathrm{n_q}$ measured outputs are available. In this case study, the identified natural frequencies and the modal assurance criteria (MAC) numbers are used as objectives for calibration of the parameters in the numerical model. The sensitivity method is based on a linearization of the output difference:

$$\boldsymbol{z}_m - \boldsymbol{z}(\boldsymbol{\theta}) \approx \boldsymbol{z}_m - (\boldsymbol{z}(\boldsymbol{\theta_i}) + \boldsymbol{G}_{i|\boldsymbol{\theta}=\boldsymbol{\theta}_i}\varDelta\boldsymbol{\theta}_i) = \boldsymbol{r}_i - \boldsymbol{G}_{i|\boldsymbol{\theta}=\boldsymbol{\theta}_i}\varDelta\boldsymbol{\theta}_i \tag{16}$$

Here, $\boldsymbol{z}_m \in \mathbb{R}^{\mathrm{n_q}}$ is the measured output and $\boldsymbol{z}(\boldsymbol{\theta})$ represents the same quantities in the FE model as a function of the parameter set $\boldsymbol{\theta} \in \mathbb{R}^{\mathrm{n_p}}$. The index i denotes a point of linearization, at which $\boldsymbol{r}_i \in \mathbb{R}^{\mathrm{n_q}}$ is the output residual:

Parameter	Type	Location	Reference value	Lower allowable change	Upper allowable change	Unit
k_x	Spring stiffness	End support	2e7	-1e7	1e10	N/m
k_y	Spring stiffness	End support	5e7	-2e7	1e10	N/m
k_z	Spring stiffness	End support	5e7	-2e7	1e10	N/m
k_{rx}	Spring stiffness	End support	0	0	1e12	Nm/rad
m_i	Mass	Pontoons	approx. 1.4e6	-2e5	2e5	kg
dz_i	Mass centre offset	Pontoons	-	-8	0	m
$I_{xx,i}$	Moment of inertia	Pontoons	approx. 1.6e8	-4e7	4e7	kgm^2
$I_{yy,i}$	Moment of inertia	Pontoons	approx. 8e7	-6e6	6e6	kgm^2
$I_{zz,i}$	Moment of inertia	Pontoons	approx. 1.6e8	-1.5e7	1.5e7	kgm^2
m_{deck}	Distributed mass	Bridge deck	135	-60	60	kg/m^2
$K_{h,z}$	Restoring stiffness	Pontoons	approx. 6e6	-1.8e5	1.8e5	N/m
$K_{h,rx,i}$	Restoring stiffness	Pontoons	approx. 4e8	-1e8	1e8	Nm/rad
μ_{steel}	Stiffness scaling	Steel superstructure	1	-0.1	0.1	-
η_{steel}	Mass scaling	Steel superstructure	1	-0.1	0.1	-
$\nu_{hydro,i}$	Hydrodynamic scaling	Pontoons	1	-0.1	0.1	-

Table 1: List of updating parameters and ranges for allowable changes.

$$\boldsymbol{r}_i = \boldsymbol{z}_m - \boldsymbol{z}(\boldsymbol{\theta_i}) \tag{17}$$

The sensitivity matrix $\boldsymbol{G} \in \mathbb{R}^{\mathrm{n_q} \times \mathrm{n_p}}$ is a Jacobian matrix. In practice, the linear system in Eq. 16 is scaled in the following way [19]:

$$\begin{bmatrix} \dfrac{z_{m,1} - z_1(\boldsymbol{\theta})}{z_{0,1}} \\ \vdots \\ \dfrac{z_{m,l} - z_l(\boldsymbol{\theta})}{z_{0,l}} \\ \vdots \\ \dfrac{z_{m,\mathrm{n_q}} - z_{\mathrm{n_q}}(\boldsymbol{\theta})}{z_{0,\mathrm{n_q}}} \end{bmatrix} = \begin{bmatrix} \dfrac{r_1}{z_{0,1}} \\ \vdots \\ \dfrac{r_l}{z_{0,l}} \\ \vdots \\ \dfrac{r_{\mathrm{n_q}}}{z_{0,\mathrm{n_q}}} \end{bmatrix} - \begin{bmatrix} \dfrac{\partial z_1}{\partial \theta_1}\dfrac{\theta_{0,1}}{z_{0,1}} & \cdots & \dfrac{\partial z_1}{\partial \theta_k}\dfrac{\theta_{0,k}}{z_{0,1}} & \cdots & \dfrac{\partial z_1}{\partial \theta_{\mathrm{n_q}}}\dfrac{\theta_{0,\mathrm{n_p}}}{z_{0,1}} \\ \vdots & & \vdots & & \vdots \\ \dfrac{\partial z_l}{\partial \theta_1}\dfrac{\theta_{0,1}}{z_{0,l}} & \cdots & \dfrac{\partial z_l}{\partial \theta_k}\dfrac{\theta_{0,k}}{z_{0,l}} & \cdots & \dfrac{\partial z_l}{\partial \theta_{\mathrm{n_q}}}\dfrac{\theta_{0,\mathrm{n_p}}}{z_{0,l}} \\ \vdots & & \vdots & & \vdots \\ \dfrac{\partial z_{\mathrm{n_q}}}{\partial \theta_1}\dfrac{\theta_{0,1}}{z_{0,\mathrm{n_q}}} & \cdots & \dfrac{\partial z_{\mathrm{n_q}}}{\partial \theta_k}\dfrac{\theta_{0,k}}{z_{0,\mathrm{n_q}}} & \cdots & \dfrac{\partial z_{\mathrm{n_q}}}{\partial \theta_{\mathrm{n_p}}}\dfrac{\theta_{0,\mathrm{n_p}}}{z_{0,\mathrm{n_q}}} \end{bmatrix} \begin{bmatrix} \dfrac{\Delta\theta_1}{\theta_{0,1}} \\ \vdots \\ \dfrac{\Delta\theta_k}{\theta_{0,k}} \\ \vdots \\ \dfrac{\Delta\theta_p}{\theta_{0,p}} \end{bmatrix} \tag{18}$$

The sub index zero indicates the normalization factors: θ_0 is a reference (initial) value of a parameter, and z_0 are either the identified natural frequency, or a constant equal to 1 for the rows which contain the MAC numbers. The scaling reduces ill-conditioning of the sensitivity matrix as well as equalizes the measured outputs such that weighting coefficients penalize relative residual errors. The objective function J is taken as a weighted sum of square errors:

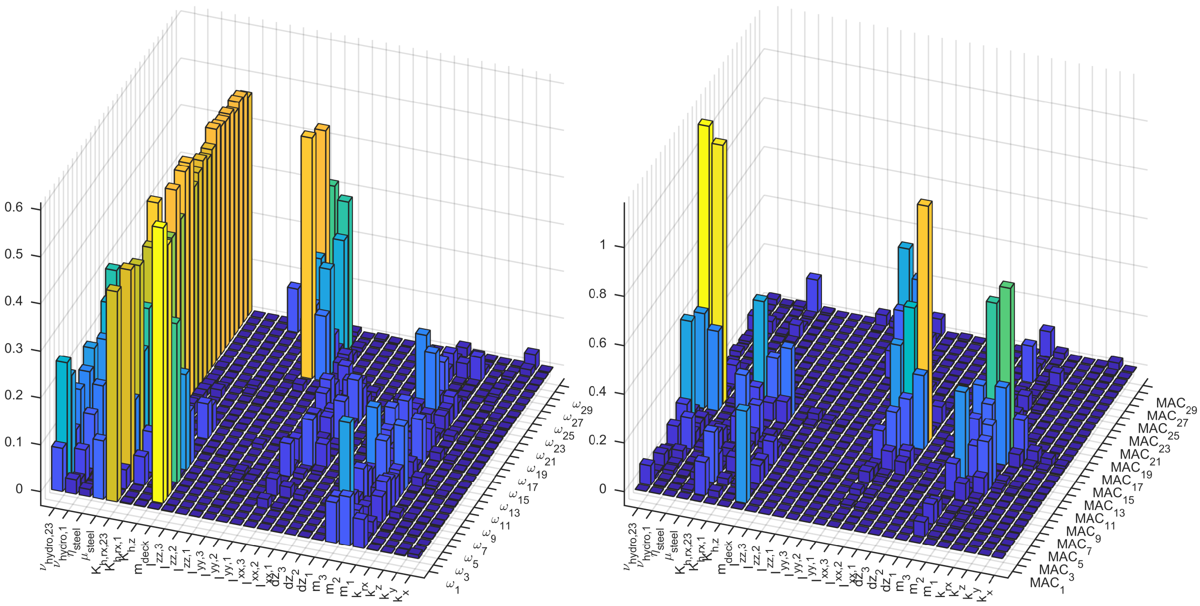

Figure 7: Normalized sensitivity of the natural frequencies and MAC-numbers with respect to the updating parameters.

$$J(\varDelta\boldsymbol{\theta}_i) = \sum_{l=1}^{\mathrm{n_q}} W_l \, (\frac{z_{m,l} - z_l(\boldsymbol{\theta})}{z_{0,l}})^2 \tag{19}$$

The weighting is chosen according to the importance and uncertainty of the measured outputs. The parameters are updated iteratively:

$$\boldsymbol{\theta}_{i+1} = \boldsymbol{\theta}_i + \varDelta\boldsymbol{\theta}_i \tag{20}$$

It is desired to constrain the parameters to a region that is considered realistic. Lower and upper bounds are enforced in the minimization problem:

$$\min J(\varDelta\boldsymbol{\theta}_i) \quad , \quad \boldsymbol{\theta}_{min} \leq \boldsymbol{\theta}_{i+1} \leq \boldsymbol{\theta}_{max} \tag{21}$$

Engineering judgement is required to set the bounds, particularly for complex cases where large uncertainties are inherent in the problem. The chosen parameter limits are presented in Table 1. Note that the listed parameters represent adjustments in the model, not total quantities. A mass, for example, can therefore attain a negative value while the total mass in that node is still greater than zero.

The sensitivity matrix for the problem is constructed analytically. A sequential perturbation of each parameter in every iteration would be too costly for the problem at hand due to the size and structure of the model. The analytical sensitivity of modal parameters in linear systems is well established in the literature. We perform a modification to accommodate for the case of frequency-dependent system matrices, which is the case for floating structures in general.

First, the sensitivity of the eigenvalues is presented, followed by the eigenvectors. Consider a system with stiffness $\boldsymbol{K}$, damping $\boldsymbol{C}$ and mass $\boldsymbol{M}$. The derivative of λ_r with respect to parameter θ_j ($j = 1, 2 \ldots \mathrm{n_p}$) can be formulated as [45]:

$$\frac{\partial \lambda_r}{\partial \theta_j} = \lambda_j \frac{\boldsymbol{\psi}_r^{\mathrm{T}}\Big[\dfrac{\partial \boldsymbol{K}}{\partial \theta_j} - \lambda_r^2 \dfrac{\partial \boldsymbol{M}}{\partial \theta_j} + i\lambda_r \dfrac{\partial \boldsymbol{C}}{\partial \theta_j}\Big]\boldsymbol{\psi}_r}{\boldsymbol{\psi}_r^{\mathrm{T}}[\lambda_r^2 \boldsymbol{M} + \boldsymbol{K}]\boldsymbol{\psi}_r} \tag{22}$$

For convenience, the definitions of the system matrices are repeated:

$$\boldsymbol{M}_r(\omega_{d,r}) = \boldsymbol{I} + \boldsymbol{\Phi}^{\mathrm{T}}\boldsymbol{M}_{\mathrm{h}}(\omega_{d,r})\boldsymbol{\Phi} + \boldsymbol{\Phi}^{\mathrm{T}}\boldsymbol{M}_{\mathrm{upd}}\boldsymbol{\Phi} \tag{23}$$

$$\boldsymbol{C}_r(\omega_{d,r}) = \boldsymbol{\Phi}^{\mathrm{T}}\boldsymbol{C}_{\mathrm{s}}\boldsymbol{\Phi} + \boldsymbol{\Phi}^{\mathrm{T}}\boldsymbol{C}_{\mathrm{h}}(\omega_{d,r})\boldsymbol{\Phi} \tag{24}$$

$$\boldsymbol{K} = \boldsymbol{\Omega}^2 + \boldsymbol{\Phi}^{\mathrm{T}}\boldsymbol{K}_{\mathrm{upd}}\boldsymbol{\Phi} \tag{25}$$

Here, the modal index r is added to indicate that every solution of Eq. 6 yields a different system mass and damping matrix. This is, once again, due to the frequency dependency inherent in the problem. Furthermore, $\boldsymbol{M}_{\mathrm{h}}(\omega)$ and $\boldsymbol{C}_{\mathrm{h}}(\omega)$ are only explicitly influenced by the parameter $\nu_{hydro,i}$. However, perturbations in any of the parameters change the natural frequencies and therefore also change $\boldsymbol{M}_{\mathrm{h}}(\omega_{d,r})$ and $\boldsymbol{C}_{\mathrm{h}}(\omega_{d,r})$ for the given mode. The sensitivity of Eq. 23-25 can therefore be written as follows:

$$\frac{\partial \boldsymbol{M}_r(\omega_{d,r})}{\partial \theta_j} = \boldsymbol{\Phi}^{\mathrm{T}}\Big[\frac{\partial \boldsymbol{M}_{\mathrm{h}}(\omega_{d,r})}{\partial \omega_{d,r}}\frac{\partial \omega_{d,r}}{\partial \theta_j} + \frac{\partial \boldsymbol{M}_{\mathrm{h}}(\omega_{d,r})}{\partial \theta_j} + \frac{\partial \boldsymbol{M}_{upd}}{\partial \theta_j}\Big]\boldsymbol{\Phi} \tag{26}$$

$$\frac{\partial \boldsymbol{C}_r(\omega_{d,r})}{\partial \theta_j} = \boldsymbol{\Phi}^{\mathrm{T}}\Big[\frac{\partial \boldsymbol{C}_{\mathrm{h}}(\omega_{d,r})}{\partial \omega_{d,r}}\frac{\partial \omega_{d,r}}{\partial \theta_j} + \frac{\partial \boldsymbol{C}_{\mathrm{h}}(\omega_{d,r})}{\partial \theta_j}\Big]\boldsymbol{\Phi} \tag{27}$$

$$\frac{\partial \boldsymbol{K}}{\partial \theta_j} = \boldsymbol{\Phi}^{\mathrm{T}}\frac{\partial \boldsymbol{K}_{upd}}{\partial \theta_j}\boldsymbol{\Phi} \tag{28}$$

Note that a dependency on $\dfrac{\partial \omega_{d,r}}{\partial \theta_j}$ emerges in Eqs. 26–27. Next, Eqs. 26-28 are substituted into Eq. 22:

$$\begin{aligned}\frac{\partial \lambda_r}{\partial \theta_j} =& \lambda_r \frac{\boldsymbol{\psi}_r^{\mathrm{T}}\boldsymbol{\Phi}^{\mathrm{T}}\Big[\dfrac{\partial \boldsymbol{K}_{upd}}{\partial \theta_j} - \lambda_r^2\Big(\dfrac{\partial \boldsymbol{M}_{upd}}{\partial \theta_j} + \dfrac{\partial \boldsymbol{M}_{\mathrm{h}}(\omega_{d,r})}{\partial \theta_j}\Big) + i\lambda_r \dfrac{\partial \boldsymbol{C}_{\mathrm{h}}(\omega_{d,r})}{\partial \theta_j}\Big]\boldsymbol{\Phi}\boldsymbol{\psi}_r}{\boldsymbol{\psi}_r^{\mathrm{T}}[\lambda_r^2 \boldsymbol{M}_r + \boldsymbol{K}]\boldsymbol{\psi}_r} \\ &+\lambda_r \frac{\boldsymbol{\psi}_r^{\mathrm{T}}\boldsymbol{\Phi}^{\mathrm{T}}\Big[-\lambda_r^2 \dfrac{\partial \boldsymbol{M}_{\mathrm{h}}(\omega_{d,r})}{\partial \omega_{d,r}} + i\lambda_r \dfrac{\partial \boldsymbol{C}_{\mathrm{h}}(\omega_{d,r})}{\partial \omega_{d,r}}\Big]\boldsymbol{\Phi}\boldsymbol{\psi}_r}{\boldsymbol{\psi}_r^{\mathrm{T}}[\lambda_r^2 \boldsymbol{M}_r + \boldsymbol{K}]\boldsymbol{\psi}_r}\frac{\partial \omega_{d,r}}{\partial \theta_j}\end{aligned} \tag{29}$$

Note that $\dfrac{\partial \omega_{d,r}}{\partial \theta_j}$ is not yet known, but is found by:

$$\omega_{d,r} = |Re(\lambda_r)| \quad , \quad \frac{\partial \omega_{d,r}}{\partial \theta_j} = |Re\Big(\frac{\partial \lambda_r}{\partial \theta_j}\Big)| \tag{30}$$

It is necessary to guess an initial value for $\dfrac{\partial \omega_{d,r}}{\partial \theta_j}$ and perform iterations of Eqs. 29 and 30. In practice, less than ten iterations are required for convergence. The sensitivity of the undamped natural frequencies is then found by:

$$\omega_r = |\lambda_r| = \sqrt{\mathrm{Re}(\lambda_r)^2 + \mathrm{Im}(\lambda_r)^2} \quad , \quad \frac{\partial \omega_r}{\partial \theta_j} = \frac{\mathrm{Re}(\lambda_r)\,\mathrm{Re}\Big(\dfrac{\partial \lambda_r}{\partial \theta_j}\Big) + \mathrm{Im}(\lambda_r)\,\mathrm{Im}\Big(\dfrac{\partial \lambda_r}{\partial \theta_j}\Big)}{\omega_r} \tag{31}$$

The eigenvectors are now considered. The natural occurrence of conjugate modal pairs in Eq. 6 is exploited. The eigenvector sensitivity is then given by [45]:

$$\frac{\partial \boldsymbol{\psi}_r}{\partial \theta_j} = -\frac{1}{2}\,\frac{\boldsymbol{\psi}_r^{\mathrm{T}}\Big[\frac{\partial \boldsymbol{M}_r(\omega_{d,r})}{\partial \theta_j} - \frac{i}{2\lambda_r}\frac{\partial \boldsymbol{C}_r(\omega_{d,r})}{\partial \theta_j}\Big]\boldsymbol{\psi}_r}{\boldsymbol{\psi}_r^{\mathrm{T}}[\boldsymbol{M}_r(\omega_{d,r}) - \frac{i}{2\lambda_r}\boldsymbol{C}_r(\omega_{d,r})]\boldsymbol{\psi}_r}\,\boldsymbol{\psi}_r + \sum_{k\neq r}^{\mathrm{n_m}}\Big[\frac{\alpha_k(\boldsymbol{\psi}_k^{\mathrm{T}}\frac{\partial \tilde{\boldsymbol{F}}_r}{\partial \theta_j}\boldsymbol{\psi}_r)\boldsymbol{\psi}_k}{\lambda_r - \lambda_k} - \frac{\alpha_k^*(\boldsymbol{\psi}_k^{*\,\mathrm{T}}\frac{\partial \tilde{\boldsymbol{F}}_r}{\partial \theta_j}^{*}\boldsymbol{\psi}_r^*)\boldsymbol{\psi}_k^*}{\lambda_r + \lambda_k^*}\Big] \tag{32}$$

where $\frac{\partial \tilde{\boldsymbol{F}}_r}{\partial \theta_j}$ and α_k are defined as follows:

$$\frac{\partial \tilde{\boldsymbol{F}}_r}{\partial \theta_j} = \Big[\frac{\partial \boldsymbol{K}_r}{\partial \theta_j} - \lambda_r^2\frac{\partial \boldsymbol{M}_r(\omega_{d,r})}{\partial \theta_j} + i\lambda_r\frac{\partial \boldsymbol{C}_r(\omega_{d,r})}{\partial \theta_j}\Big] \tag{33}$$

$$\alpha_k = \frac{1}{\boldsymbol{\psi}_k^{\mathrm{T}}[2\lambda_k\boldsymbol{M}_k(\omega_{d,k}) - \boldsymbol{i}\boldsymbol{C}_k(\omega_{d,k})]\boldsymbol{\psi}_k} \tag{34}$$

A modification of these expressions is not necessary; the FSI is implicitly accounted for when Eqs. 23–28 are used in Eqs. 32– 34. A relation with the MAC number sensitivity is sought. The MAC between analytical mode number r and an identified mode $\boldsymbol{a}_s \in \mathbb{C}^{\mathrm{n_d}}$ is:

$$\mathrm{MAC}_{rs} = \frac{\boldsymbol{a}_s^{\mathrm{H}}\,\boldsymbol{v}_r\,\boldsymbol{v}_r^{\mathrm{H}}\,\boldsymbol{a}_s}{\boldsymbol{v}_r^{\mathrm{H}}\,\boldsymbol{v}_r\,\boldsymbol{a}_s^{\mathrm{H}}\,\boldsymbol{a}_s} \quad , \quad \boldsymbol{v}_r = \boldsymbol{\Phi}^{acc}\boldsymbol{\psi}_r \tag{35}$$

where $\boldsymbol{\Phi}^{acc} \in \mathbb{R}^{\mathrm{n_d}\times\mathrm{n_m}}$ is the subrows of $\boldsymbol{\Phi}$ at the DOFs of the accelerometers. The MAC sensitivity is then found by differentiating Eq. 35:

$$\frac{\partial \mathrm{MAC}_{rs}}{\partial \theta_j} = \frac{\boldsymbol{a}_s^{\mathrm{H}}\,(\dfrac{\partial \boldsymbol{v}_r}{\partial \theta_j}\boldsymbol{v}_r^{\mathrm{H}} + \boldsymbol{v}_r\dfrac{\partial \boldsymbol{v}_r^{\mathrm{H}}}{\partial \theta_j})\,\boldsymbol{a}_s\boldsymbol{v}_r^{\mathrm{H}}\boldsymbol{v}_r - \boldsymbol{a}_s^{\mathrm{H}}\boldsymbol{v}_r\boldsymbol{v}_r^{\mathrm{H}}\boldsymbol{a}_s\,(\dfrac{\partial \boldsymbol{v}_r^{\mathrm{H}}}{\partial \theta_j}\boldsymbol{v}_r + \boldsymbol{v}_r^{\mathrm{H}}\dfrac{\partial \boldsymbol{v}_r}{\partial \theta_j})}{(\boldsymbol{v}_r^{\mathrm{H}}\boldsymbol{v}_r)^2(\boldsymbol{a}_s^{\mathrm{H}}\boldsymbol{a}_s)} \quad , \quad \frac{\partial \boldsymbol{v}_r}{\partial \theta_j} = \boldsymbol{\Phi}^{acc}\frac{\partial \boldsymbol{\psi}_r}{\partial \theta_j} \tag{36}$$

This concludes the establishment of the analytical sensitivity matrix when natural frequencies and MAC numbers are used as updating objectives.

5. System identification and output weighting

The locations of the 14 tri-axial accelerometers are shown in Fig. 2. The monitoring system installed at the bridge is further described in [40]. A total of $\mathrm{n_d}$ = 42 acceleration outputs were available for system identification. A 90 minute long time series recorded on 8 November 2015 was selected for acquiring the model updating output

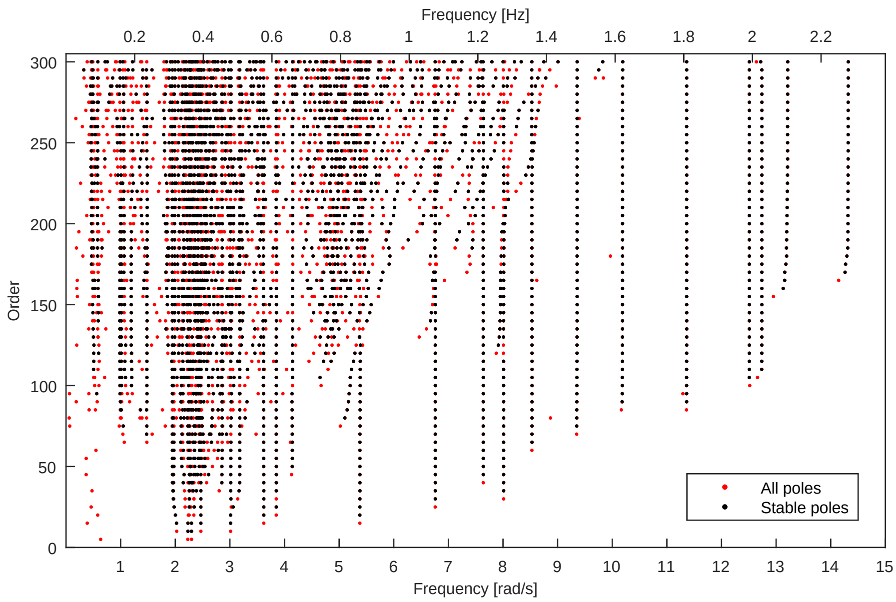

Figure 8: Stabilization diagram for Cov-SSI when 100 block rows are used.

parameters. The wave elevation recorded in this period indicates a significant wave height varying between 0.4 and 0.65 m, while the ten minute mean wind was between 8 and 16 m/s. System identification was performed using covariance-driven and data-driven stochastic subspace identification (Cov-SSI and DD-SSI [46]) and frequency-domain decomposition (FDD [47]). The acceleration data, originally sampled at 200 Hz, were low-pass filtered using a Chebyshev type II filter with a cut-off frequency of 5 Hz and then resampled to 10 Hz. For the FDD, the power spectral density was estimated using a Welch average. Using SSI, a number of identifications were performed with different time lags because all the modes are not equally well identified using the same set of algorithmic parameters. The modes were then selected accordingly, where it was believed that a fair consistency in the poles occurred. The 30 modes that were identified are listed in Table 2. SSI, which assumes a white noise input realization, has the drawback that false poles tend to occur at dominant frequencies of the load [48]. For this case, the poles of the modes in the frequency range of the wave loading therefore experience inconsistencies or bias of varying degrees. The stabilization diagram in Fig. 8 shows that many poles in the range 1-5 rad/s are spurious. From Fig. 9, which show the singular values of the acceleration spectrum, it is also clear it is difficult to distinguish the peaks in the low frequency range. The estimation errors or "noise" manifest to a larger extent in estimated mode shapes, and the natural frequencies are observed to be more consistent across different model orders and time lags.

Note that due to noise, the choice of weighting coefficients in the objective function affects the optimization results. Ideally, the weighting should be assigned with regard to uncertainties, i.e. more uncertain outputs should be assigned smaller weights. At the same time, selected natural frequencies or mode shapes are often sought to be prioritized (weighted higher), e.g. a good representation of a few modes is often considered to be important. In

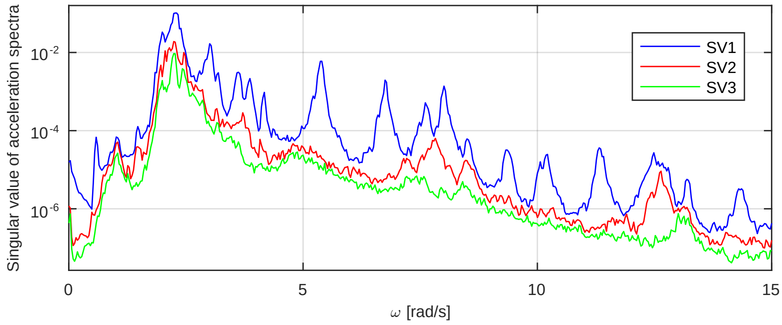

Figure 9: The three largest singular values of acceleration spectra.

Mode no. s	$\bar{\omega}_s$ [rad/s]	Identification method	Mode no. s	$\bar{\omega}_s$ [rad/s]	Identification method
1	0.5862	Cov-SSI	16	3.620	Cov-SSI
2	0.9810	DD-SSI	17	3.851	Cov-SSI
3	1.012	DD-SSI	18	4.149	Cov-SSI
4	1.055	DD-SSI	19	5.382	Cov-SSI
5	1.187	Cov-SSI	20	6.759	Cov-SSI
6	1.345	FDD	21	7.639	Cov-SSI
7	1.481	Cov-SSI	22	8.012	Cov-SSI
8	1.946	DD-SSI	23	8.531	Cov-SSI
9	1.974	Cov-SSI	24	9.358	Cov-SSI
10	2.112	DD-SSI	25	10.187	Cov-SSI
11	2.249	DD-SSI	26	11.364	Cov-SSI
12	2.472	DD-SSI	27	12.510	Cov-SSI
13	2.857	DD-SSI	28	12.742	Cov-SSI
14	3.017	DD-SSI	29	13.207	DD-SSI
15	3.181	DD-SSI	30	14.322	DD-SSI

Table 2: Identified modes

practice, when noise is present and a priori uncertainty information is not available, firm engineering judgement is necessary. For the presented case, the lower half of the listed modes primarily contribute to the dynamic response. On the one hand, it is desired to sternly penalize errors in the lower modes because these are most integral for future applications of the updated model. On the other hand, as discussed above, these modes are more prone to noise, which may severely contaminate the estimated updating parameters. The opposite is also true; the higher modes are viewed as less important in the updated model but are believed to be better identified. The sketched weighting coefficients are shown in Fig. 10. Natural frequencies are considered to be more important and more reliable than MAC numbers. Note that there are alternative approaches, such as multi-objective optimization [49, 50], in which a set of optimal solutions is obtained. Further information on managing uncertainties in model updating is extensively covered in [1].

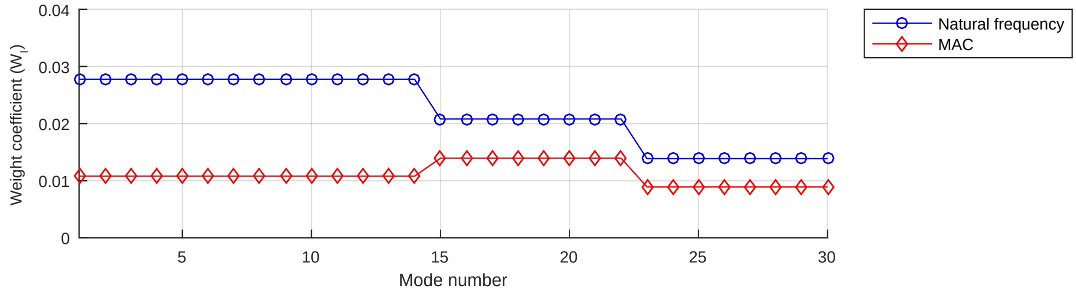

Figure 10: Weighting in the objective function. The coefficients sum to unity.

6. Updating results and discussion

The MATLAB function *lsqlin* with a trust-region algorithm is used to solve the constrained least squares problem defined in Eq. 21. Initially, the parameters are free to take large steps, and the step bounds are made smaller as the objective becomes closer to convergence. Note that the system is overdetermined ($\mathrm{n_q} = 60 > 27 = \mathrm{n_p}$), which is preferred to avoid non-unique solutions.

Since the natural frequencies are very closely spaced, the modes are initially not necessarily in the correct order. A mode matching is necessary before the minimum of the objective function (Eq. 19) can be found. Here, the combined measure

$$(1-\gamma)\,\mathrm{MAC}_{rs} - \gamma\,\frac{|\bar{\omega}_s - \omega_r|}{\bar{\omega}_s} \tag{37}$$

with $\gamma = 0.5$ was an useful indicator; high values indicates a match between an identified mode (s) and a model mode (r). However, we experienced the largest matching difficulties not in the iterations but at the initial point. In particular, higher modes are sensitive to the bearing stiffness, which has a high degree of uncertainty. Initially, a clear match was not observed for four of the identified modes. A manual adjustment to stiffen the bearings was required to produce a definite match; however, even in this case, engineering judgement control was essential to confirm that the pairing was reasonable. After an initial match in the first iteration is successful, the model quickly adapts, and the quantity in Eq. 37 becomes a definite metric for distinguishing the modes.

Nine iterations were performed until a fair stabilization in the objective function was reached. The objective function decreased from 16.4e-3 to 2.98e-3. The updated frequencies and MAC numbers are listed in Table 3. Prior to the update, the mean frequency error was 3.23%, which was reduced to 2.34%. The largest initial errors were observed for mode 10 (+10.22%), mode 14 (+8.59%), mode 16 (+8.83%) and mode 17 (+11.59%). The updating reduced these errors considerably, but they are still the largest frequency discrepancies. Other than the four mentioned modes, no clear trend was observed regarding whether the initial model is too stiff or too soft. Unfortunately, the error also increased for some modes.

An updated MAC plot is presented in Fig. 11. Three pairs of modes, namely, 10/11, 14/15 and 17/18, appear

Mode no. s	Measured $\bar{\omega}_s$	Initial ω_r (error)		Updated ω_r (error)		Initial MAC	Updated MAC (change)	
1	0.586	0.587	(0.15%)	0.580	(-1.05%)	0.987	0.987	(≈ 0)
2	0.981	1.001	(2.01%)	0.987	(0.61%)	0.819	0.816	(-0.004)
3	1.012	1.039	(2.64%)	1.032	(1.97%)	0.936	0.935	(≈ 0)
4	1.055	1.086	(2.98%)	1.050	(-0.41%)	0.742	0.787	(+0.045)
5	1.187	1.193	(0.50%)	1.175	(-1.00%)	0.801	0.839	(+0.037)
6	1.349	1.358	(0.67%)	1.379	(2.22%)	0.834	0.820	(-0.014)
7	1.481	1.480	(-0.07%)	1.449	(-2.18%)	0.939	0.939	(≈ 0)
8	1.946	1.919	(-1.40%)	1.878	(-3.51%)	0.954	0.980	(+0.026)
9	1.974	1.947	(-1.38%)	1.951	(-1.16%)	0.917	0.939	(+0.023)
10	2.112	2.328	(10.22%)	2.246	(6.31%)	0.865	0.830	(-0.035)
11	2.249	2.104	(-6.42%)	2.225	(-1.06%)	0.585	0.909	(+0.323)
12	2.472	2.454	(-0.75%)	2.409	(-2.56%)	0.984	0.978	(-0.006)
13	2.857	2.839	(-0.62%)	2.763	(-3.26%)	0.958	0.953	(-0.005)
14	3.017	3.276	(8.59%)	3.167	(4.97%)	0.987	0.978	(-0.009)
15	3.181	2.975	(-6.48%)	3.106	(-2.34%)	0.949	0.967	(+0.018)
16	3.620	3.940	(8.83%)	3.874	(7.02%)	0.693	0.986	(+0.293)
17	3.851	4.297	(11.59%)	4.134	(7.37%)	0.973	0.982	(+0.009)
18	4.149	4.036	(-2.74%)	4.056	(-2.25%)	0.331	0.963	(+0.631)
19	5.382	5.227	(-2.87%)	5.258	(-2.29%)	0.981	0.987	(+0.006)
20	6.759	6.615	(-2.14%)	6.720	(-0.58%)	0.984	0.983	(-0.002)
21	7.639	7.506	(-1.74%)	7.315	(-4.23%)	0.983	0.984	(+0.001)
22	8.012	7.952	(-0.75%)	7.894	(-1.47%)	0.978	0.974	(-0.003)
23	8.531	8.402	(-1.51%)	8.530	(-0.01%)	0.970	0.971	(+0.001)
24	9.358	9.107	(-2.69%)	9.294	(-0.68%)	0.954	0.956	(+0.001)
25	10.187	9.895	(-2.86%)	10.121	(-0.65%)	0.960	0.969	(+0.009)
26	11.364	11.130	(-2.06%)	11.312	(-0.45%)	0.955	0.955	(≈ 0)
27	12.510	12.474	(-0.28%)	12.306	(-1.63%)	0.948	0.966	(+0.018)
28	12.742	12.580	(-1.28%)	12.704	(-0.30%)	0.874	0.975	(+0.100)
29	13.207	12.713	(-3.74%)	13.585	(2.86%)	0.571	0.953	(+0.383)
30	14.322	13.310	(-7.07%)	14.864	(3.79%)	0.588	0.877	(+0.289)

Table 3: Natural frequencies and MAC numbers before and after updating.

off-diagonal, which testifies to the closeness in frequency. Generally, the MAC numbers were less sensitive than the natural frequencies. Of the 30 modes, the MAC numbers improved more than 0.01 for 12 modes and decreases more than 0.01 for two modes. For the remainder, the absolute difference was less than 0.01. Mode 10 decreased the most (-0.035), whereas the largest improvement was observed for mode 11 (+0.323), mode 16 (+0.293), mode 18 (+0.631), mode 29 (+0.383) and mode 30 (+0.289). The lowest MAC values were found for modes 2, 4, 6 and 10, which are not surprisingly modes with a high susceptibility to noise in the identification process. In fact, many of the lower modes tended to have low MAC numbers. Apart from the problems of accuracy in modal identification, the lower modes

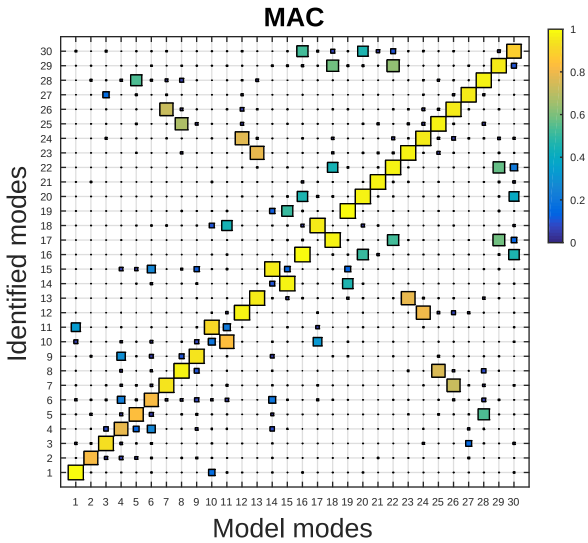

Figure 11: MAC numbers between the identified and modelled modes for the updated model.

were highly influenced by the FSI. A high hydrodynamic contribution means that errors in hydrodynamics matrices particularly transfer to these modes. As shown in Fig. 4, the rate of change in $\boldsymbol{M}_{\mathrm{h}}(\omega)$ was also large around $\omega = 1$ rad/s, which, in practical terms, translates to a higher degree of uncertainty for modes in this frequency range.

The updated parameters are shown in Table 4. The stiffness of the bearing springs increased substantially, except in the x-direction, where the axial rod (cf. Fig. 5) already provides support. Since the springs in general display a low sensitivity (cf. Fig 7), large changes are required for the spring parameters to influence the modal properties. In the initial model, the stiffness of the neoprene pads was roughly estimated. Embedded steel plates can also contribute to increased stiffness. In addition, the geometries of the bearings are in reality more complex than in the model; it is therefore expected that the modelled springs represents the mechanical behaviour but do not replicate the bearings at a detailed level.

Many of the parameters are related to uncertainties at the pontoons. A problem emerges when a distinction between two parameters is sought. For example, the pontoon point mass m_i can compensate for an erroneous hydrodynamic mass and vice versa. A looser interpretation of what a parameter represents may be necessary. The updated inertia of the pontoons likely contains corrections in the hydrodynamic mass. For pontoon type 3, the modelled concrete mass is 1480 tonnes, and the hydrodynamic mass is on the order of magnitude 100 and 4000 tonnes for the y (lateral) and z (vertical) directions, respectively. The point mass corrections are $m_1 = 136$ tonnes, $m_2 = -138$ tonnes and $m_3 = 148$ tonnes. It is unrealistic that the concrete mass as built should deviate by up to 10% from the drawings. The mass corrections must therefore be viewed as a whole between the concrete pontoons and the hydrodynamic mass. The same holds for the moments of inertia. I_{zz} has less influence than I_{xx} and I_{yy} and therefore reaches the limit

Parameter	Updated value (change)	Reference in initial model	Reference value	Change [%]
k_x	-5.90e+06	Bearing spring	2.00e+07	-29.5
k_y	1.64e+08	Bearing spring	5.00e+07	328.5
k_z	8.04e+07	Bearing spring	5.00e+07	160.8
k_{rx}	2.09e+09	Bearing spring	0.00e+00	N/A
m_1	1.06e+05	Mass pontoon type 1	1.47e+06	7.2
m_2	-1.38e+05	Mass pontoon type 2	1.39e+06	-9.9
m_3	1.48e+05	Mass pontoon type 3	1.48e+06	10.0
$d_{z,1}$	≈ 0	-	-	-
$d_{z,2}$	-4.71	-	-	-
$d_{z,3}$	≈ 0	-	-	-
$I_{xx,1}$	-7.38e+06	I_{xx} pontoon type 1	1.65e+08	-4.5
$I_{xx,2}$	7.53e+06	I_{xx} pontoon type 2	1.47e+08	5.1
$I_{xx,3}$	9.99e+06	I_{xx} pontoon type 3	1.61e+08	6.2
$I_{yy,1}$	-5.56e+06	I_{yy} pontoon type 1	9.02e+07	-6.2
$I_{yy,2}$	5.08e+05	I_{yy} pontoon type 2	7.75e+07	0.7
$I_{yy,3}$	-4.49e+06	I_{yy} pontoon type 3	8.11e+07	-5.5
$I_{zz,1}$	-2.53e+06	I_{zz} pontoon type 1	1.89e+08	-1.3
$I_{zz,2}$	1.50e+07	I_{zz} pontoon type 2	1.76e+08	8.5
$I_{zz,3}$	1.50e+07	I_{zz} pontoon type 3	1.88e+08	8.0
$K_{h,z}$	-1.80e+05	Restoring stiffness pontoon types 1, 2, 3	5.97e+06	-3.0
$K_{h,rx,1}$	7.46e+07	Restoring rot. stiffness pontoon type 1	3.57e+08	20.9
$K_{h,rx,23}$	-1.70e+07	Restoring rot. stiffness pontoon types 2, 3	4.00e+08	-4.2
η_{steel}	-0.0640	Steel superstructure	1.0000	-6.4
μ_{steel}	-0.0619	Steel superstructure	1.0000	-6.2
m_{deck}	-59.91	Asphalt	135.00	-44.4
$\nu_{hydro,1}$	-0.0227	Hydrodynamic properties pontoon type 1	1.0000	-2.3
$\nu_{hydro,23}$	0.0170	Hydrodynamic properties pontoon types 2, 3	1.0000	1.7

Table 4: Values of updated parameters and comparison with reference values in the initial model

of approximately 8% of the pontoon moment of inertia in the initial model. This issue points to a major robustness challenge encountered in FE model updating of complex structures. As an alternative, the parameters related to the same node could be merged. Here, however, this was not considered an option since the hydrodynamic mass is special (frequency dependent, non-uniform) compared to the structural mass.

The frequency dependency in the FSI brings further challenges to the updating. Here, uncertainties in hydrodynamic mass and damping were only represented by a global scaling factor ($\nu_{hydro,i}$). It might be that the hydrodynamic mass for one particular frequency is accurate but incorrect at an other frequency. The frequency dimension adds a level of complexity that is difficult to handle. Ideally, the hydrodynamic mass could be parametrized further, e.g. by parameterizing each DOF or calibrating the hydrodynamic mass at each natural frequency. The parameters $\nu_{hydro,1}$ and $\nu_{hydro,23}$ are both on the order of 2%.

The stiffness of the steel superstructure highly influenced all the modes. A stiffness reduction of 6.4% was reached. This result is within reasonable uncertainty limits considering not only the material properties but also general simplifications from representing the truss with beam elements. The truss joints are modelled with full fixity, i.e. the beams are continuous through the joints. A softer degree of fixity can occur in reality. The steel superstructure might be better represented by a lower elastic modulus. On the other hand, the beams are modelled centre-to-centre joint, whereas the effective beam lengths in reality are shorter. The non-structural distributed mass on the bridge deck is reduced by 60 kg/m^2, which corresponds to a 44% reduction of the initially modelled asphalt layer. A 6.2% reduction of the steel mass is also obtained. $K_{h,z}$ also reaches the lower limit. The limit should not be extended since it is unrealistic that the buoyancy should deviate more than 3%. The restoring stiffness, however, is far more uncertain, and it is here seen to change up to 20.9 %.

Overall, caution should be taken in accepting the updated parameter set as definite physical quantities, not only because the result generally depends on the choice of output residual weighting. Since many of the parameters affect the system similarly, many combinations of parameters can solve the optimization problem equally well from a practical perspective.

Note that the updating also improved the results for applications of inverse response prediction of using data measured at the bridge. Furthermore, note that prior to updating, the model was first modified manually to closer resemble the specifications of the structural drawings. Among the modifications was adding non-structural mass, refining the end support geometry, detailing the boundary conditions and re-estimating the pontoon inertia. This effort also improved the model before the updating scheme was implemented.

7. Conclusion

FE model updating as a methodology for calibrating numerical models is a field that is still in development. The application of model updating to suspension bridges and cable-stay bridges is well represented in the literature. However, no attempts have been made to update a floating bridge model. This paper presents a case study of the sensitivity method in FE model updating with application to the Bergsøysund Bridge, a floating pontoon bridge. In floating structures, the fluid interaction governs the dynamic behaviour. Commonly, this can be modelled by including frequency-dependent added hydrodynamic mass and damping matrices obtained from software based on linearized potential theory. The established model of the bridge combines an FE model of the structure with the added hydrodynamic matrices. A technique for establishing an analytical sensitivity matrix was shown, taking the frequency-dependent system matrices of the model into account.

A system identification of the bridge was performed using data from 14 triaxial accelerometers. Thirty global modes with natural frequencies in the range $0.58 - 14.3$ rad/s were identified. The relative errors in natural frequencies and MAC numbers between the modelled and identified modes were used as objectives for calibration. A total of 27 parameters were selected to reflect the model components believed to be uncertain and that also had an influence on the dynamic characteristics. After 9 iterations with the sensitivity method were performed, the largest initial errors in natural frequencies and MAC numbers were improved. The average natural frequency error was decreased from 3.23% to 2.34%. In general, the largest initial errors were improved, but not all errors were reduced. The MAC numbers generally improved or did not change significantly; the updated MAC numbers ranged from 0.79 to 0.98.

The case study demonstrated that numerical models of large floating bridge can be improved by FE updating, but many practical challenges still exist. A general improvement of the modal characteristics is possible. Further reduction of the errors, however, requires a significant reduction of noise and a refinement of the updating parameters. When several parameters are related to the same node, for instance, the structural pontoon mass and hydrodynamic mass, it is challenging to practically distinguish these parameters from each other because different combinations of these parameters may solve the minimization problem equally well. The choice of weighting coefficients in the objective function will affect the end results, particularly when noise (bias) is present in the natural frequencies and MAC numbers from the system identification. Therefore, engineers must make an error penalty selection that reflects both the uncertainties and the prioritization of selected modes, which often becomes a job of trial and error.

This study also demonstrates the challenge of matching the identified and model modes when natural frequencies are very closely spaced. Here, both utilizing MAC numbers and comparing natural frequencies is vital. In addition, it was observed that the initial model must sufficiently represent the structure for an initial match to succeed, which is an issue since the initial model often contains errors.

Acknowledgements

This work was supported by the Norwegian Public Roads Administration. The constructive comments of three anonymous reviewers improved the paper significantly.

References

[1] E. Simoen, G. De Roeck, G. Lombaert, Dealing with uncertainty in model updating for damage assessment: A review, Mechanical Systems and Signal Processing 56 (2015) 123–149.

[2] C.-P. Fritzen, D. Jennewein, T. Kiefer, Damage detection based on model updating methods, Mechanical systems and signal processing 12 (1) (1998) 163–186.

[3] S. W. Doebling, C. R. Farrar, M. B. Prime, et al., A summary review of vibration-based damage identification methods, Shock and vibration digest 30 (2) (1998) 91–105.

[4] J. M. Brownjohn, P.-Q. Xia, H. Hao, Y. Xia, Civil structure condition assessment by FE model updating: methodology and case studies, Finite elements in analysis and design 37 (10) (2001) 761–775.

[5] J. M. W. Brownjohn, P. Moyo, P. Omenzetter, Y. Lu, Assessment of highway bridge upgrading by dynamic testing and finite-element model updating, Journal of Bridge Engineering 8 (3) (2003) 162–172.

[6] J. M. Brownjohn, P.-Q. Xia, Dynamic assessment of curved cable-stayed bridge by model updating, Journal of Structural Engineering 126 (2) (2000) 252–260.

[7] P. G. Bakir, E. Reynders, G. De Roeck, Sensitivity-based finite element model updating using constrained optimization with a trust region algorithm, Journal of Sound and Vibration 305 (1) (2007) 211–225.

[8] A. Teughels, G. De Roeck, Structural damage identification of the highway bridge Z24 by FE model updating, Journal of Sound and Vibration 278 (3) (2004) 589–610.

[9] A. Teughels, G. De Roeck, Damage assessment of the Z24 bridge by FE model updating, in: Key engineering materials, vol. 245, Trans Tech Publ, 19–26, 2003.

[10] E. Reynders, G. D. Roeck, P. Gundes Bakir, C. Sauvage, Damage identification on the Tilff Bridge by vibration monitoring using optical fiber strain sensors, Journal of engineering mechanics 133 (2) (2007) 185–193.

[11] J. Mottershead, M. Friswell, Model updating in structural dynamics: a survey, Journal of sound and vibration 167 (2) (1993) 347–375.

[12] A. Berman, E. Nagy, Improvement of a large analytical model using test data, AIAA journal 21 (8) (1983) 1168–1173.

[13] Q. Zhang, C. Chang, T. Chang, Finite element model updating for structures with parametric constraints, Earthquake engineering & structural dynamics 29 (7) (2000) 927–944.

[14] J. Wu, Q. Li, Finite element model updating for a high-rise structure based on ambient vibration measurements, Engineering Structures 26 (7) (2004) 979–990.

[15] X.-h. He, Z.-w. Yu, Z.-q. Chen, Finite element model updating of existing steel bridge based on structural health monitoring, Journal of Central South University of Technology 15 (2008) 399–403.

[16] M. Huang, W. Guo, H. Zhu, L. Li, Dynamic test and finite element model updating of bridge structures based on ambient vibration, Frontiers of Architecture and Civil Engineering in China 2 (2) (2008) 139–144.

[17] D. A. Rade, G. Lallement, A strategy for the enrichment of experimental data as applied to an inverse eigensensitivity-based FE model updating method, Mechanical Systems and Signal Processing 12 (2) (1998) 293–307.

[18] R. Cantieni, Updating of analytical models of existing large structures based on modal testing, in: Recent Advances in Bridge Engineering. Proceedings of the US-Europe Workshop on Bridge Engineering., 1996.

[19] J. E. Mottershead, M. Link, M. I. Friswell, The sensitivity method in finite element model updating: a tutorial, Mechanical systems and signal processing 25 (7) (2011) 2275–2296.

[20] M. Link, Updating of analytical models: a review of numerical procedures and application aspects, in: Proc., Structural Dynamics Forum SD2000, Los Alamos, 1999.

[21] W.-X. Ren, S.-E. Fang, M.-Y. Deng, Response surface–based finite-element-model updating using structural static responses, Journal of Engineering Mechanics 137 (4) (2010) 248–257.

[22] W.-X. Ren, H.-B. Chen, Finite element model updating in structural dynamics by using the response surface method, Engineering Structures 32 (8) (2010) 2455–2465.

[23] S. Chakraborty, A. Sen, Adaptive response surface based efficient finite element model updating, Finite Elements in Analysis and Design 80 (2014) 33–40.

[24] B. Asgari, S. A. Osman, A. Adnan, Sensitivity analysis of the influence of structural parameters on dynamic behaviour of highly redundant cable-stayed bridges, Advances in Civil Engineering 2013.

[25] J. R. Casas, Dynamic testing and model updating of cable-stayed bridges, in: Society for Experimental Mechanics, Inc, 16 th International Modal Analysis Conference., vol. 2, 1360–1366, 1998.

[26] B. A. Zárate, J. M. Caicedo, Finite element model updating: Multiple alternatives, Engineering Structures 30 (12) (2008) 3724–3730.

[27] Q. Zhang, T. Chang, C. Chang, Finite-element model updating for the Kap Shui Mun cable-stayed bridge, Journal of Bridge Engineering 6 (4) (2001) 285–293.

[28] Y. Ding, A. Li, Finite element model updating for the Runyang Cable-stayed Bridge tower using ambient vibration test results, Advances in Structural Engineering 11 (3) (2008) 323–335.

[29] F. Benedettini, C. Gentile, Operational modal testing and FE model tuning of a cable-stayed bridge, Engineering Structures 33 (6) (2011) 2063–2073.

[30] R. N. Merce, G. N. Doz, J. Brito, J. H. Macdonald, M. I. Friswell, Finite element model updating of a suspension bridge using ANSYS software, in: Inverse Problems, Design and Optimization Symposium, 16–18, 2007.

[31] A. L. Hong, F. Ubertini, R. Betti, Wind analysis of a suspension bridge: identification and finite-element model simulation, Journal of Structural Engineering 137 (1) (2010) 133–142.

[32] R. Zhong, Z. Zong, J. Niu, Q. Liu, P. Zheng, A multiscale finite element model validation method of composite cable-stayed bridge based on Probability Box theory, Journal of Sound and Vibration 370 (2016) 111–131.

[33] Q. Zhu, Y. Xu, X. Xiao, Multiscale modeling and model updating of a cable-stayed bridge. I: Modeling and influence line analysis, Journal of Bridge Engineering 20 (10) (2014) 04014112.

[34] H. Schlune, M. Plos, K. Gylltoft, Improved bridge evaluation through finite element model updating using static and dynamic measurements, Engineering structures 31 (7) (2009) 1477–1485.

[35] D. Ribeiro, R. Calçada, R. Delgado, M. Brehm, V. Zabel, Finite element model updating of a bowstring-arch railway bridge based on experimental modal parameters, Engineering Structures 40 (2012) 413–435.

[36] B. Jaishi, W.-X. Ren, Structural finite element model updating using ambient vibration test results, Journal of Structural Engineering 131 (4) (2005) 617–628.

[37] T. Zordan, B. Briseghella, T. Liu, Finite element model updating of a tied-arch bridge using Douglas-Reid method and Rosenbrock optimization algorithm, Journal of Traffic and Transportation Engineering (English Edition) 1 (4) (2014) 280–292.

[38] X. Xiao, Y. Xu, Q. Zhu, Multiscale modeling and model updating of a cable-stayed bridge. II: Model updating using modal frequencies and influence lines, Journal of Bridge Engineering 20 (10) (2014) 04014113.

[39] E. Watanabe, T. Utsunomiya, Analysis and design of floating bridges, Progress in Structural Engineering and Materials 5 (3) (2003) 127–144.

[40] K. A. Kvåle, O. Øiseth, Structural monitoring of an end-supported pontoon bridge, Marine Structures 52 (2017) 188–207.

[41] K. A. Kvåle, R. Sigbjörnsson, O. Øiseth, Modelling the stochastic dynamic behaviour of a pontoon bridge: A case study, Computers & Structures 165 (2016) 123–135.

[42] K. A. Kvåle, O. Øiseth, A. Rønnquist, R. Sigbjörnsson, Modal Analysis of a Floating Bridge Without Side-Mooring, in: Dynamics of Civil Structures, Volume 2, Springer, 127–136, 2015.

[43] Ø. W. Petersen, O. Øiseth, T. S. Nord, E. Lourens, Model-Based Estimation of Hydrodynamic Forces on the Bergsoysund Bridge, in: Proceedings of the 34th IMAC, A Conference and Exposition on Structural Dynamics, Dynamics of Civil Structures, Volume 2, Springer, 217–228, 2016.

[44] A. Naess, T. Moan, Stochastic dynamics of marine structures, Cambridge University Press, 2012.

[45] S. Adhikari, Rates of change of eigenvalues and eigenvectors in damped dynamic system, AIAA journal 37 (11) (1999) 1452–1458.

[46] C. Rainieri, G. Fabbrocino, Output-only Modal Identification, in: Operational Modal Analysis of Civil Engineering Structures, Springer, 103–210, 2014.

[47] R. Brincker, L. Zhang, P. Andersen, Modal identification of output-only systems using frequency domain decomposition, Smart materials and structures 10 (3) (2001) 441.

[48] B. Peeters, G. De Roeck, Stochastic system identification for operational modal analysis: a review, Journal of Dynamic Systems, Measurement, and Control 123 (4) (2001) 659–667.

[49] R. Perera, A. Ruiz, A multistage FE updating procedure for damage identification in large-scale structures based on multiobjective evolutionary optimization, Mechanical Systems and Signal Processing 22 (4) (2008) 970–991.

[50] K. Christodoulou, E. Ntotsios, C. Papadimitriou, P. Panetsos, Structural model updating and prediction variability using Pareto optimal models, Computer methods in applied mechanics and engineering 198 (1) (2008) 138–149.